

This is an Open Access document downloaded from ORCA, Cardiff University's institutional repository:<https://orca.cardiff.ac.uk/id/eprint/80784/>

This is the author's version of a work that was submitted to / accepted for publication.

Citation for final published version:

Haynes, Brittany, Zhang, Yanhua, Liu, Fangchao, Li, Jing, Petit, Sarah, Kothayer, Hend, Bao, Xun, Westwell, Andrew D. , Mao, Guangzhao and Shekhar, Malathy P.V. 2016. Gold nanoparticle conjugated Rad6 inhibitor induces cell death in triple negative breast cancer cells by inducing mitochondrial dysfunction and PARP-1 hyperactivation: Synthesis and characterization. *Nanomedicine: Nanotechnology, Biology and Medicine* 12 (3) , pp. 745-757. 10.1016/j.nano.2015.10.010

Publishers page: <http://dx.doi.org/10.1016/j.nano.2015.10.010>

Please note:

Changes made as a result of publishing processes such as copy-editing, formatting and page numbers may not be reflected in this version. For the definitive version of this publication, please refer to the published source. You are advised to consult the publisher's version if you wish to cite this paper.

This version is being made available in accordance with publisher policies. See <http://orca.cf.ac.uk/policies.html> for usage policies. Copyright and moral rights for publications made available in ORCA are retained by the copyright holders.



Gold nanoparticle conjugated Rad6 inhibitor induces cell death in triple negative breast cancer cells by inducing mitochondrial dysfunction and PARP-1 hyperactivation: Synthesis and characterization

Brittany Haynes^{1,2,§}, Yanhua Zhang^{3,§}, Fangchao Liu³, Jing Li^{1,2}, Sarah Petit^{1,2}, Hend Kothayer⁴, Xun Bao¹, Andrew D Westwell⁴, Guangzhao Mao^{3,*}, and Malathy PV Shekhar^{1,2,5*}

¹Karmanos Cancer Institute, 110 E. Warren Avenue, Detroit, MI 48201

²Department of Oncology, ⁵Department of Pathology Wayne State University School of Medicine, 110 E. Warren Avenue, Detroit, MI 48201

³Department of Chemical Engineering and Materials Science, Wayne State University College of Engineering, 5050 Anthony Wayne Drive, Detroit, MI 48202

⁴School of Pharmacy and Pharmaceutical Sciences, Cardiff University, Redwood Building, King Edward VII Avenue, Wales, CF10 3NB, U.K.

Running Title: Rad6 inhibitor gold nanoparticles for anticancer delivery

Key words: Gold nanoparticles, Rad6, Poly(ADP-ribose) polymerase (PARP-1), lysosome, mitochondria, autophagy

[§]Contributed equally

*Address correspondence to:

Malathy Shekhar, Department of Oncology, Wayne State University School of Medicine, Tumor Microenvironment Program, Karmanos Cancer Institute, Detroit, Michigan 48201, U.S.A., Tel. (313) 578-4326; E mail: shekharm@karmanos.org.

Guangzhao Mao, Department of Chemical Engineering and Materials Science, Wayne State University College of Engineering, 5050 Anthony Wayne Drive, Detroit, MI 48202, U.S.A., Tel. (313) 577-3804; E-mail: gzmao@eng.wayne.edu

Word count:

Abstract: 150

Body of text and figure legends: 4,996

Number of References: 51

Number of figures: 8

Abstract

We recently developed a small molecule inhibitor SMI#9 for Rad6, a protein overexpressed in aggressive breast cancers and involved in DNA damage tolerance. SMI#9 induces cytotoxicity in cancerous cells but spares normal breast cells; however, its therapeutic efficacy is limited by poor solubility. Here we chemically modified SMI#9 to enable its conjugation and hydrolysis from gold nanoparticle (GNP). SMI#9-GNP and parent SMI#9 activities were compared in mesenchymal and basal triple negative breast cancer (TNBC) subtype cells. Whereas SMI#9 is cytotoxic to all TNBC cells, SMI#9-GNP is endocytosed and cytotoxic only in mesenchymal TNBC cells. SMI#9-GNP endocytosis in basal TNBCs is compromised by aggregation. However, when combined with cisplatin, SMI#9-GNP is imported and synergistically increases cisplatin sensitivity. Like SMI#9, SMI#9-GNP spares normal breast cells. The released SMI#9 is active and induces cell death via mitochondrial dysfunction and PARP-1 stabilization/hyperactivation. This work signifies the development of a nanotechnology-based Rad6-targeting therapy for TNBCs.

Introduction

The human homologues of yeast Rad6, HHR6A and HHR6B (referred as Rad6A and Rad6B) play a fundamental role in DNA damage tolerance pathway (1-4), and the ubiquitin conjugating (UBC) activity of Rad6 is essential for this function (5, 6). The Rad6B homologue is weakly expressed in normal breast cells but overexpressed in metastatic and chemoresistant breast carcinomas (7-9). Constitutive overexpression of Rad6B in nontransformed human breast epithelial cells induces tumorigenesis and resistance to cisplatin and doxorubicin (7, 10, 11). Conversely, Rad6B silencing renders cells chemosensitive (11), implicating the relevance of Rad6 in transformation and drug resistance, and the potential therapeutic benefit of inhibiting Rad6. We have recently reported the development of a novel Rad6-selective small molecule inhibitor SMI#9 that inhibits Rad6 UBC activity (12). SMI#9 treatment suppresses proliferation and migration, and induces apoptosis in breast cancer cells but spares normal breast cells (12). However, SMI#9 has poor aqueous solubility that limits its therapeutic efficacy. Here we developed a drug delivery system that would improve its solubility and uptake.

Gold nanoparticles (GNPs) are ideal drug delivery scaffolds because they are nontoxic and nonimmunogenic (13,14), and have good biocompatibility and stability (15). Surface modification allows GNPs to be readily functionalized with multiple agents including chemotherapy, oligonucleotides and proteins making them good delivery vehicles (16). Several GNP-based drugs have been developed by CytImmune with their lead drug Aurimune (TNF α bearing PEGylated gold nanoparticles) in clinical trials (17).

Here we report the synthesis of SMI#9-tethered GNPs using a chemistry that allows intracellular release of SMI#9. SMI#9-GNPs were characterized for size and ligand conjugation, and intracellular release of conjugated SMI#9 by Fourier transform infrared spectroscopy (FTIR)

and liquid chromatography coupled tandem mass spectrometry (LC-MS/MS). Intracellular uptake, localization, cytotoxicity and molecular responses to SMI#9-GNP were evaluated in triple negative breast cancer (TNBC) cells as TNBCs represent a heterogeneous disease with poor clinical outcomes and few targeted therapy options as they lack estrogen receptor, progesterone receptor and Her2/neu amplification. We analyzed the responses to conjugated and free SMI#9 in mesenchymal and basal subtypes as they represent the two major TNBC subtypes (18). We show that the mesenchymal subtype is sensitive to SMI#9-GNP and that modified SMI#9 released from GNP acts similarly to unconjugated parent SMI#9.

Methods

Synthesis of gold nanoparticle (GNP) and conjugation of Rad6 inhibitor SMI#9 to GNP

SMI#9 was synthesized as previously described (12). The steps for GNP and SMI#9 nanoconjugation are described in Scheme 1 (19-23), and details are provided under Supplementary Materials.

Characterization of GNP and GNP-drug conjugates

SMI#9 conjugated to GNP was characterized by thermogravimetric analysis (TGA) on a SDT-Q600 Thermo-Gravity Analyser using air as the supporting gas. The air flow rate was maintained at 100 ml/min, and sample heated from 25 to 800°C at a rate of 10°C/min. GNP solutions were also characterized by UV-vis spectroscopy with a Varian Cary[®] 50 spectrometer in 2 mm optical path cells, and by transmission electron microscopy (TEM) at 200 kV with a JEOL JEM-2010 microscope equipped with a Gatan multiscan CCD camera. TEM samples were prepared by placing a droplet of the GNP solution on a Formvar-coated copper grid. Dynamic light scattering (DLS) and zeta potential were measured using a Malvern Nano-ZS. The Z-

average hydrodynamic diameter (HD), polydispersity index (PDI), and zeta potential were measured at 25°C. 15 scans were performed in each measurement. The backscattering angle Θ was fixed at 172° with a laser wavelength $\lambda = 633$ nm. The size measurement range was set between 1 nm and 6 μm . HD is a function of the diffusion coefficient (D), temperature (T), and

viscosity (η) according to the Stokes-Einstein equation:
$$\frac{HD}{kT} = \frac{3\pi\eta D}{}$$
, k is Boltzmann constant, T is 25 °C, and D was obtained from autocorrelation function via the cumulant fitting. Atomic force microscopy (AFM) imaging was conducted using a Dimension 3100 AFM from VEECO. AFM tapping mode in liquid was used and the nanoconjugate was deposited on mica by spin coating.

Cell survival assay

MDA-MB-231, SUM-1315, MDA-MB-468, and HCC1937 TNBC cells (ATCC) were maintained in Dulbecco's Modified Eagle's Medium (DMEM)/F-12 supplemented with 5% fetal bovine serum. Nontransformed MCF10A human breast cells were maintained in DMEM/F12 supplemented with 5% horse serum, 20 ng/ml epidermal growth factor, 10 $\mu\text{g}/\text{ml}$ insulin, 0.5 $\mu\text{g}/\text{ml}$ hydrocortisone and 0.10 $\mu\text{g}/\text{ml}$ cholera toxin (7). SMI#9-GNP sensitivity was assessed by trypan blue staining or MTT assay. Cells ($5-7 \times 10^3$) were seeded in 96-well plates and treated with free SMI#9, SMI#9-GNP, or blank-GNP at various concentrations in triplicates for 72 h. In some cases, cells were treated singly with 0.1-10 μM cisplatin or in combination with SMI#9-GNP. On the final day, medium was replaced with drug-free medium, and incubated with MTT for 2-3 h. MTT-formazan crystals were dissolved in 0.04 N HCl/isopropanol and absorbance measured at 570 nm using the Synergy 2 microplate reader. Alternately, cultures were

trypsinized and cell viability was determined by trypan blue exclusion using the Biorad TC10 automatic cell counter. At least three independent experiments were performed for each cell line.

SMI#9 and SMI#9-GNP uptake and intracellular release of the free drug from GNP conjugate

MDA-MB-231 (3×10^5) cells were plated in 35 mm dishes and exposed to various doses of SMI#9-GNP or untreated for 24-48 h. Cultures were rinsed, lysed by freeze-thaw cycles in cold hypotonic buffer, and clarified by centrifugation at 10,000 g. Aliquots of clarified lysates were analysed by FTIR spectroscopy using control lysates spiked with free SMI#9 as reference. To determine intracellular release of modified SMI#9 from nanoparticles, SUM1315 (2×10^6 cells/100 mm dish) cells were exposed for 8 or 24 h to 5 μM free SMI#9, 5 μM SMI#9-GNP or the corresponding amount of blank-GNP, or untreated. Cultures were rinsed in ice-cold phosphate buffered saline (PBS), lysed with cold 80% methanol and clarified by centrifugation at 10,000 g for 10 min at 4°C (24). Aliquots of supernatants were subjected to high performance liquid chromatography (HPLC) coupled with tandem mass spectrometry (LC-MS/MS) analysis. Chromatography was performed with Waters Model 2695 system and Waters Xterra MS C18 column (50 x 2.1 mm i.d., 3.5 μm) using an isocratic mobile phase of methanol/0.45% formic acid in water (60:30, v/v) at a flow rate of 0.2 mL/min. The column effluent was monitored using a Waters Quattro Micro™ triple quadrupole mass-spectrometric detector. Multiple reaction monitoring at positive ionization mode were chosen for the analyte detection. Mass spectrometric parameters were optimized for detection of SMI#9 with the cone voltage of 45 V and collision energy of 24 V. Samples were introduced into the ionization source through a heated nebulized probe (350 °C) with 500 L/hr desolvation nitrogen gas flow. For SMI#9

detection, the spectrometer was programmed to monitor transition of the parent ion m/z 366.69 ($[M+H]^+$) to the major daughter ion with m/z 150.1 (Fig. 3A, b). For the detection of modified SMI#9 released from GNP, the spectrometer was programmed to monitor transition of the parent ion m/z 397.3 to the major daughter ion m/z 150.1. We monitored 14 MS transitions m/z 366.69 > 150.1, 368.86 > 150.7, 381.3 > 150.1, 381.3 > 150.7, 381.3 > 232.3, 381.3 > 248.3, 397.3 > 150.1, 397.3 > 150.7, 397.3 > 232.3, 397.3 > 248.3, 379.4 > 150.1, 379.4 > 150.7, 379.4 > 232.3, and 379.4 > 248.3 to determine release of modified SMI#9 from the GNP conjugates. All the chosen parent ions were selected in the first quadrupole and allowed to pass into the collision cell filled with argon gas with a pressure of 0.00172 mBar. The dwell time per channel was set to 0.01s for data collection.

Acridine orange/ethidium bromide staining

Breast cancer cells (10×10^3) were seeded on cover slips and treated with vehicle, free SMI#9, blank-GNP or SMI#9-GNP for 24-48 h. Cover slips were rinsed with PBS, stained with ethidium bromide/acridine orange (each 25 μ g/ml), and immediately imaged with an Olympus BX40 fluorescence microscope. A minimum of six fields with at least 50 cells/field were scored for determination of dye uptake (12), and experiments were repeated at least three times.

Mitochondrial assay

The impact of free SMI#9 or SMI#9-GNP on mitochondrial membrane potential ($\Delta\psi_m$) on SUM1315 and HCC1937 TNBC cells was assessed using JC-1 (Mitocapture, Biovision, Mountainview, CA), a potentiometric green fluorescent dye that shifts to red fluorescence within mitochondria with a normal negative $\Delta\psi_m$. Briefly, cells were incubated with the MitoCapture reagent for 15 min at 37°C and imaged by fluorescence microscopy (25). The percent of cells

showing >5 punctate J-aggregates were scored by counting three-five fields of 50-100 cells in each field. To quantitate mitochondrial membrane potential changes, 20 X 10³ SUM1315 or HCC1937 cells were seeded in 96-well plate, and treated for 48 h with 5 µM SMI#9-GNP or blank-GNP. Cells were then incubated with 10 µM JC-1 for 30-60 min, and the red and green fluorescence intensities of JC-1 were measured at Excitation/Emission = 490/525 nm and 490/590 nm with a Synergy 2 fluorescence reader. Results were expressed as the ratio of red to green fluorescence.

Intracellular uptake of SMI#9-GNP

To examine localization of SMI#9-GNP transported into lysosomes, SUM1315 or HCC1937 cells were seeded on sterile coverslips and treated with blank- or SMI#9-GNP. Cultures were rinsed and incubated in LysoSensor Green DND-189 (75 nM) for 30-60 min at 37°C (26). Cells were counterstained with 4',6-diamidino-2-phenylindole (DAPI) to localize the nucleus and images were acquired with an Olympus BX40 fluorescence microscope equipped with a Sony high resolution/sensitivity camera.

Western blot and immunofluorescence analysis

Breast cancer cells treated with vehicle, free SMI#9, blank- or SMI#9-GNP (1-5 µM) for 24-96 h were lysed (12), and aliquots of lysates containing 25 µg of protein were subjected to SDS-PAGE and western blot analysis of PARP-1 (Cell Signaling), Rad6 (7), LC3-I/II (Cell Signaling), p62 (Cell Signaling) and β-actin (Sigma). To determine LC3 or p62 subcellular localization, control or SMI#9-GNP treated cells were fixed with methanol:acetone (1:1, v/v) and stained with

anti-LC3 or anti-p62 antibody. Slides were incubated with FITC- or Texas Red-conjugated anti-rabbit secondary antibody, counterstained with DAPI, and analyzed by fluorescence microscopy.

Statistical analysis

Each experiment was performed in triplicate and reproduced at least three times. Data are expressed as mean \pm S.D, and P <0.05 determined by Student's t-test was considered to be statistically significant.

Results

Nanoparticle synthesis and characterization

For the production of SMI#9-tethered GNPs, citrate-reduced GNPs were synthesized from HAuCl₄.3H₂O and subsequently capped by MSA. Modified SMI#9 was attached to the MSA-GNP surface via ester bond (Scheme 1). The chemical compositions of GNP and SMI#9-GNP were determined by TGA. Figure 1A shows the TGA curves of MSA-GNP (blank-GNP) and MSA-GNP conjugated SMI#9 (SMI#9-GNP) with weight loss of 6.15% and 13%, respectively, at 800°C. The detailed calculations for loading and coverage of modified SMI#9 on MSA-GNP are provided under Supplementary data. Figure 1B shows the UV-vis spectra of GNPs before and after conjugation with modified SMI#9. The surface plasmon resonance (SPR) absorption peak of freshly prepared GNPs is 508 nm, which corresponds to GNP diameter range of 3-5 nm. However, upon conjugation with modified SMI#9, the SPR absorption peak broadened and shifted to 524 nm, which is indicative of particle aggregation. The size of SMI#9-GNPs was also determined by TEM (Fig. 1C) and AFM (Fig. 1D) which showed a size of 32 nm and 40.2 \pm 1.4 nm, respectively, that is consistent with aggregation. DLS further verified the average size of

SMI#9-GNP nanoconjugate at 41 nm as compared to 4.8 nm for GNP. The zeta potential of MSA-capped GNP changed from -41 mV to -16.2 mV after conjugation with SMI#9. The decrease in surface charge is the result of SMI#9 conjugation to highly charged MSA. Particle aggregation could also contribute to surface charge reduction.

Intracellular SMI#9-GNP uptake and release

To determine SMI#9-GNP uptake and intracellular release of the conjugated SMI#9, MDA-MB-231 or SUM1315 cells were exposed to SMI#9-GNP, blank-GNP, SMI#9 or untreated, and cell lysates analyzed by FTIR or LC-MS/MS. Control cell lysates spiked with (parent) SMI#9 were included as reference controls. FTIR analysis of SMI#9 (Fig. 1E), and lysates prepared from SMI#9-GNP treated MDA-MB-231 cells or MDA-MB-231 control lysates spiked with SMI#9 showed the characteristic nitro group banding at $\sim 1550\text{ cm}^{-1}$, indicative of SMI#9 presence (Fig. 1F).

SMI#9 was hydroxymethylated to enable conjugation to GNP via an ester bond (Scheme 1 and Fig. 2A, a). Intracellular hydrolysis would result in release of modified SMI#9 with the molecular weight of 396.3, which would produce parent ions at 397.3 ($[\text{M}+\text{H}]^+$) and product ions at 150.1 (Fig. 2A, b and c). A strong peak was detected under m/z 381.3 $>$ 150.1 transition (but not under 397.3 $>$ 150.1) at both 8 and 24 h in SMI#9-GNP treated cells that was not detected in blank-GNP or untreated control cultures (Fig. 2C). Release of drug with 381.3 molecular mass could arise by dehydroxylation of hydroxymethylated-SMI#9. The precise structure of intracellularly released drug and its metabolic processing is under investigation. The peak signals were stronger at 8 h as compared to 24 h, suggesting rapid intracellular processing. The positive control cells treated with free (parent) SMI#9 showed the expected peak under m/z 366.69 $>$

150.1 transition (Fig. 2B). These results suggest efficient uptake and rapid intracellular processing of the chemically modified SMI#9-GNP conjugates.

Cellular response to SMI#9-conjugated GNP

The sensitivities of MDA-MB-231, SUM1315, HCC1937, and MDA-MB-468 TNBC cells, and nontransformed MCF10A human breast cells to SMI#9-GNP as compared to blank-GNP or free (parent) SMI#9 were determined by MTT or trypan blue staining assays. Whereas all TNBC cell lines are growth inhibited by free SMI#9 with GI50s for MDA-MB-231, SUM1315, HCC1937 and MDA-MB-468 of 5 μ M, 6 μ M, 1.8 μ M and 3 μ M, respectively, these cell lines display variable sensitivities to SMI#9-GNP (Fig. 3A-3D). Blank-GNP added at amounts equivalent to 1 or 10 μ M SMI#9-GNP demonstrated negligible cytotoxicity in all four lines. MCF10A cells were unaffected by free SMI#9 (12) and SMI#9-GNP (Fig. 3E). Among the TNBC lines, SUM1315 cells displayed greatest sensitivity to SMI#9-GNP with GI50 (based on SMI#9 concentration) of ~0.5 μ M as compared to 8.2 μ M for MDA-MB-231 cells. Both HCC1937 and MDA-MB-468 cells were unaffected by SMI#9-GNP. Consistent with the MTT assay results, simultaneous phase-contrast imaging showed drug-induced morphologic transformations in the sensitized cells (Fig. 3G). In HCC1937 (and MDA-MB-468, data not shown) cells that are unaffected by SMI#9-GNP, the GNPs appeared to aggregate at the cell surface (Fig. 3G). When combined with cisplatin, however, SMI#9-GNP synergistically increased cisplatin sensitivity of MDA-MB-468 and HCC1937 cells (Fig. 3F). These data suggest that once imported into the cells, SMI#9-GNP is therapeutically active in basal subtype TNBC cells.

SMI#9-GNP sensitivity is associated with apoptosis

Since MTT assays (Fig. 3A-3D) showed variable SMI#9-GNP induced growth inhibitory effects in the TNBC lines, we verified whether these sensitivities resulted from cytostatic or cytotoxic responses. Cells undergoing apoptosis/necrosis were detected by the differential uptake of the fluorescent DNA binding dyes acridine orange and ethidium bromide. Consistent with MTT data (Fig. 3A), SMI#9 and SMI#9-GNP treatments triggered morphological changes consistent with apoptosis in SUM1315 cells (Fig. 4A). Early apoptosis marked by intercalated acridine orange within fragmented DNA (27) and late stages of apoptosis marked by apoptotic body separation and presence of reddish-orange color due to acridine orange binding to fragmented DNA (28) were observed in SUM1315 cells treated with SMI#9-GNP (Fig. 4A, 4C). SUM1315 cells treated with blank-GNP (at amounts equivalent to 5 μ M SMI#9-GNP) were minimally affected as >98% of the cells showed a green intact nuclear structure (Fig. 4A, 4C). Acridine orange/ethidium bromide staining of MDA-MB-231 cells showed similar SMI#9-GNP induced morphological changes (data not shown). Consistent with the MTT data (Fig. 3C), acridine orange/ethidium bromide staining showed morphological alterations consistent with apoptosis in SMI#9-treated but not SMI#9-GNP treated, confirming SMI#9-GNP insensitivity of HCC1937 cells (Fig. 4B, 4D).

SMI#9-GNP sensitive TNBC cells show altered mitochondrial membrane potential

Since the results of acridine orange/ethidium bromide staining showed dye uptake consistent with apoptosis in SMI#9-GNP sensitive cells, we tested whether this occurred by a mitochondrial-regulated mechanism. Alterations in mitochondrial transmembrane potential were evaluated in SUM1315 and HCC1937 cells treated with free SMI#9, blank-GNP, or SMI#9-GNP

using the JC-1 assay. $\Delta\psi_m$ is a marker of mitochondrial function and is used to monitor loss of mitochondrial function. JC-1 (5,5',6,6'-tetrachloro-1,1',3,3'-tetraethylbenzimidazolylcarbocyanine iodide) is a lipophilic cationic dye which depending upon $\Delta\psi_m$ accumulates in the cytoplasm as a green monomer or as punctate red aggregates in hyperpolarized mitochondria of cancer cells (29). The negative charge established by the mitochondrial membrane potential allows the lipophilic cationic dye to enter mitochondria where it accumulates (30). When a critical concentration is exceeded, J-aggregates form, which fluoresces red. In apoptotic cells, $\Delta\psi_m$ collapses, and the JC-1 is unable to accumulate in mitochondria. JC-1 thus remains in the cytoplasm as a green fluorescent monomer. Untreated or blank-GNP treated control SUM1315 and HCC1937 cells show heterogeneous punctate red and green fluorescence (Fig. 4E, 4F). Overnight treatment with 1 μ M free SMI#9 reduced J-aggregate formation in both SUM1315 and HCC1937 cells (Fig. 4E, 4F). Mitochondrial membrane depolarization consistent with a shift in fluorescence emission of JC-1 from red to green, and occasional cells with mislocalized punctate red signals were observed in SMI#9-treated HCC1937 cells (Fig. 4F). However, consistent with MTT and acridine orange/ethidium bromide staining data, $\Delta\psi_m$ of HCC1937 cells were unaffected by SMI#9-GNP treatment (Figs. 4F). In contrast, the mitochondrial integrities of SUM1315 cells treated with free SMI#9 and SMI#9-GNP were similarly and dramatically compromised (Figs. 4E). Quantitation of mitochondrial activity by manual scoring of J-aggregates (Figs. 4G, 4H) and fluorescence measurements of red and green forms of JC-1 (Fig. 4I) further confirmed that SMI#9-induced cell death occurs from loss of mitochondrial function, and importantly free and conjugated SMI#9 behave similarly to inhibit mitochondrial function and cell viability.

Lysosomal uptake of SMI#9-GNP

Since SUM1315 and HCC1937 breast cancer cells displayed different sensitivities to SMI#9-GNP while maintaining similar cellular sensitivities to free SMI#9, we hypothesized that these variations arose from differences in uptake rather than intracellular processing as combination with cisplatin enhanced SMI#9-GNP uptake and cisplatin sensitivity (Fig. 3F). Internalization of nanoparticles in general is accomplished by endocytosis, transfer of cargo to early and mature endosomes, and fusion to become late endosomes/lysosomes (31-33). Control or SMI#9-GNP treated SUM1315 or HCC1937 cells were stained with LysoSensor Green DND-189 to label the lysosomes and the presence of aggregated GNP cargo examined. LysoSensor Green DND-189 is an acidotropic dye that accumulates in intracellular acidic organelles as a result of protonation and has a fluorescence intensity that is proportional to acidity (34, 35). SMI#9-GNP is efficiently internalized into SUM1315 cells as evidenced by the presence of GNP aggregates in lysosomes marked by the LysoSensor Green DND-189 dye (Fig. 5B). The overlapping of lysosomes with GNP aggregates and the strong sensitivity of SUM1315 cells to SMI#9-GNP suggest potential hydrolysis of the ester bond linked SMI#9-GNP and release of conjugated SMI#9 as supported by LC-MS/MS (Fig. 2). Although both control and SMI#9-GNP treated SUM1315 cells showed robust staining with the lysosomal marker (Fig. 5A and 5B), formation of “acidic vesicles” (potentially indicative of autolysosome formation, a key feature of autophagy), was observed only in SMI#9-GNP treated SUM1315 cells (compare Figs. 5A' and 5B'). In contrast, HCC1937 cells showed weak staining with LysoSensor Green (Fig. 5C and 5D) suggesting weak acidification.

SMI#9-induced cell death is associated with PARP-1 stabilization

Since SMI#9 treatment induces apoptosis by causing mitochondrial dysfunction, we analyzed the steady-state levels of PARP-1 protein in TNBC cells treated for 24 h with vehicle, free SMI#9, blank-GNP or SMI#9-GNP. As shown in Fig. 6A, each cell line displayed unique PARP-1 processing blueprints, which was unaffected by blank-GNP and SMI#9-GNP. However, treatment with free SMI#9 for 24 h resulted in PARP-1 stabilization/hyperactivation. Accumulation of PARP-1 containing heterogeneous chain lengths of poly ADP-ribose (PARylated PARP-1) was observed in all cell lines, and appear to result from alterations in PARP-1 processing (Fig. 6A). Since 24 h treatment with SMI#9-GNP did not evoke similar changes in PARP-1, we performed PARP-1 analysis in SUM1315 cells treated with SMI#9-GNP for 24-96 h. The results in Fig. 6B show that like free SMI#9, SMI#9-GNP also induces PARP-1 activation as evidenced by time-dependent accumulation of high molecular weight PARP-1 forms after 24 h. These data suggest that both free and conjugated SMI#9 exert similar molecular effects on PARP-1 activation; however, GNP-conjugated SMI#9 requires longer time to elicit this effect.

The conversion of the soluble form of LC3 (LC3-I) to the lipidated and autophagosome-associated form (LC3-II) is considered a hallmark of autophagy (36). High basal levels of LC3-I and LC3-II were observed in MDA-MB-231 cells compared to SUM1315 cells, suggesting the involvement of autophagic flux in normal survival of these cells (Fig. 6B). Treatment for 24 h with free SMI#9 but not SMI#9-GNP downregulated both LC3-I and LC3-II in MDA-MB-231 cells (Fig. 6B). Although changes in LC3-I processing was not readily apparent in SUM1315 cells treated for 24 h with free SMI#9 or SMI#9-GNP, a dramatic increase in LC3-I to LC3-II conversion that was commensurate with PARP-1 hyperactivation was observed at 48 and 96 h of

treatment (Fig. 6B). These effects are selective for SMI#9-GNP since treatment with blank-GNP for up to 96 h produced no changes in LC-3-I/II ratios or PARP-1 activation (Fig. 6B). p62 is degraded through the autophagy-lysosomal pathway and is mediated by interaction with LC3 (37,38). Concomitant with SMI#9-GNP-induced increases in LC3-I to LC3-II conversion, p62 protein steady-state levels were decreased confirming autophagy induction (Fig. 1 in Supplementary Results). Consistent with these data, LC3-positive dots were detected by immunofluorescence staining only in SMI#9-GNP treated SUM1315 cells (Fig. 6D, arrow), whereas strongly stained p62-positive bodies were detected in control cells but not in SMI#9-GNP treated cells (Fig. 6E). The coincident increases in PARP-1 hyperactivation, LC-I to LC3-II conversion, and p62 decrease in SMI#9-GNP treated cells signify cell death that is further supported by MTT assays (Fig. 3A), phase-contrast micrographs (Figs. 3G, 6C), and the presence of lysosome-associated acidic vesicles (Fig. 5B', arrows) in SMI#9-GNP treated but not control cells. Rad6 steady-state levels were marginally increased in SMI#9-GNP treated cells (Fig. 6B). Since Rad6 activity is inhibited under these conditions, these data suggest an important role for Rad6 activity in assuring survival of cancer cells.

Discussion

In this paper, we have developed a GNP-based vehicle for delivering SMI#9, and demonstrated that the tethered chemically modified SMI#9 is released from GNP and that it acts similar to the parent SMI#9. Whereas both basal and mesenchymal subtypes of TNBCs are sensitized by free (parent) SMI#9, we discovered that unlike the mesenchymal TNBC subtype (SUM1315 and MDA-MB-231) cells that are sensitive to SMI#9-GNP, the basal TNBC subtype

(MDA-MB-468 and HCC1937) cells are refractory to SMI#9-GNP. We show that the higher efficacy of SMI#9-GNP in SUM1315 and MDA-MB-231 cells results from efficient endocytosis and lysosomal processing of SMI#9-tethered GNP. SMI#9-GNP uptake and cellular response are compromised in HCC1937 and MDA-MB-468 cells due to aggregation at the cell surface. Theoretical models predict the optimal diameter for GNP uptake to be ~50 nm in receptor-mediated endocytosis (39-41). The larger aggregates found in HCC1937 and MDA-MB-468 cells may require more interactions to enable wrapping of membrane around the aggregates (39,40,42). It should be noted that although all TNBC cells were cultured under similar conditions and with similar amounts of SMI#9-GNP, SMI#9-GNP aggregation occurred only in the basal subtype, suggesting local microenvironment involvement in particle aggregation.

These data are corroborated by LysoSensor Green DND-189 staining which showed SMI#9-GNP localization in strongly fluorescing lysosomes of SUM1315 cells, whereas similar staining of HCC1937 and MDA-MB-468 cells showed weak LysoSensor Green fluorescence. LysoSensor Green DND-189 is an acidotropic dye that accumulates in intracellular acidic organelles as a result of protonation and has a fluorescence intensity that is proportional to acidity (34, 35). Ma et al. (43) recently reported a GNP size-dependent alkalinization of lysosomes, which is consistent with the presence of large SMI#9-GNP aggregates and weak fluorescence of LysoSensor Green DND-189 dye in HCC1937 and MDA-MB-468 cells. On a broad scale, we observed that in the mesenchymal TNBC subtype where SMI#9-GNP exists in a monodispersed or lower order of aggregation, SMI#9-GNP is endocytosed efficiently and hydrolyzed to release the conjugated drug. Although SMI#9-GNP uptake is impaired in basal subtype TNBC cells, when combined with cisplatin treatment SMI#9-GNP is effectively imported as it synergistically enhances cisplatin sensitivity. These data implicate the universal

applicability of SMI#9-GNP in treatment of TNBCs as treatment regimens generally employ combination therapies. Rad6 is overexpressed in TNBC cells and expressed weakly in normal cells (6, 44). Since MCF10A cells are unaffected by both free and GNP-conjugated SMI#9 suggests that SMI#9-GNP may be used to deliver therapy to cancer cells while sparing the normal cells.

Our mechanistic studies show that both SMI#9 and SMI#9-GNP induce apoptosis by affecting mitochondrial integrity. A role for Rad6 in the maintenance of healthy mitochondria was recently reported (45). Here the authors showed that the UBC activity of Rad6A in combination with Parkin E3 ubiquitin ligase ubiquitinates mitochondrial proteins to facilitate autophagic clearance of dysfunctional mitochondria (45). Patient derived human Rad6A mutant cells with defective UBC activity had accumulation of defective mitochondria (45). Since SMI#9 targets Rad6 UBC activity, and cells treated with free or GNP-tethered SMI#9 show accumulation of dysfunctional mitochondria not only corroborate Rad6 role in mitochondrial function but also provide mechanistic evidence for SMI#9-GNP functionality. Treatment of TNBC cells with SMI#9 induces apoptosis, autophagy and necrosis. Based on our data, we have formulated a model (Fig. 7) that could explain cell death caused by Rad6 inhibition. Rad6 along with Parkin facilitates the removal of dysfunctional mitochondria by autophagy. Thus the low levels of autophagy in control cells promote cell survival by eliminating damaged organelles and preventing apoptosis. SMI#9 treatment causes accumulation of damaged mitochondria which triggers upregulation of autophagy, an attempt by the cells to clear damaged organelles and rescue cell survival. However, excessive autophagy combined with mitochondrial permeabilization induces apoptosis as it promotes the release of apoptogenic factors involved in caspase-dependent or caspase-independent cell death. Our study showed that in both SMI#9- and

SMI#9-GNP-induced apoptosis, PARP-1 cleavage is not observed. Rather PARP-1 is stabilized/hyperactivated indicating caspase-independent apoptosis (46-48) and necrosis from energy depletion (49,50). Since both Rad6 loss (45) and PARP-1 hyperactivation (51) are associated with mitochondrial dysfunction, and inhibition of Rad6 by SMI#9 induces both mitochondrial dysfunction and PARP-1 activation, our data implicate a potential novel role for Rad6 linking these processes.

In summary, the mechanistic data presented here show that GNP is a suitable vehicle for delivering SMI#9 and that the chemically modified SMI#9 released from GNP functions similarly as the free parent SMI#9. Our data also show distinct differences in uptake and tolerability of SMI#9-GNP between basal and mesenchymal subtypes of TNBC cells that emanate from cell-specific microenvironment-induced effects on SMI#9-GNP aggregation. Although the SMI#9-GNP aggregates are nontoxic, these data are significant because it illustrates how cell microenvironments can induce alterations in the physical properties of GNP-drug conjugates and influence their anti-cancer efficacies.

Acknowledgements

This work was been supported by grants R21CA178117 from the National Cancer Institute (to MPS), a Molecular Therapeutics Program Grant from Karmanos Cancer Institute (to MPS and GM), and CHE1404285 and R01HD031550 grants (to GM) from the National Science Foundation and National Institutes of Health, respectively. BH was supported by Initiative for Maximizing Student Diversity (IMSD) award GM058905 and Ruth L. Kirschstein National Research Service Award T32-CA009531 training grants from NIH.

References

1. Koken MH, Smit EM, Jaspers-Dekker I, Oostra BA, Hagemeijer A, Bootsma D, et al. Localization of two human homologs, HHR6A and HHR6B, of the yeast DNA repair gene RAD6 to chromosomes Xq24-q25 and 5q23-q31. *Genomics*, 1992;12:447-53.
2. Koken MH, Reynolds P, Jaspers-Dekker I, Prakash L, Prakash S, Bootsma D, et al. Structural and functional conservation of two human homologs of the yeast DNA repair gene RAD6. *Proc Natl Acad Sci U S A* 1991;88:8865-9.
3. Lawrence CW. Mutagenesis in *Saccharomyces cerevisiae*. *Adv Genet* 1982; 21:173-254.
4. Jentsch S, McGrath JP, Varshavsky A. The yeast DNA repair gene RAD6 encodes a ubiquitin-conjugating enzyme. *Nature* 1987;329:131-4.
5. Sung P, Prakash S, Prakash L. Mutation of cysteine-88 in the *Saccharomyces-Cerevisiae* Rad6 protein abolishes its ubiquitin-conjugating activity and its various biological functions. *Proc Natl Acad Sci U S A* 1990;87:2695-9.
6. Sung P, Prakash S, Prakash L. Stable ester conjugate between the *Saccharomyces cerevisiae* RAD6 protein and ubiquitin has no biological activity. *J Mol Biol* 1991;221:745-9.
7. Shekhar MP, Lyakhovich A, Visscher DW, Heng H, Kondrat N. Rad6 overexpression induces multinucleation, centrosome amplification, abnormal mitosis, aneuploidy, and transformation. *Cancer Res* 2002;62:2115-24.
8. Shekhar MPV, Biernat LA, Pernick N, Tait L, Abrams J, Visscher DW. Utility of DNA postreplication repair protein Rad6B in neoadjuvant chemotherapy response. *Med Oncol* 2010;27:466-73.

9. Gerard B, Sanders MA, Visscher DW, Tait L, Shekhar MPV. Lysine 394 is a novel Rad6B-induced ubiquitination site on beta-catenin. *Biochim Biophys Acta - Mol Cell Res* 2012; **1823**:1686-96.
10. Lyakhovich A, Shekhar MP. RAD6B overexpression confers chemoresistance: RAD6 expression during cell cycle and its redistribution to chromatin during DNA damage-induced response. *Oncogene* 2004;23:3097-106.
11. Lyakhovich A, Shekhar MP. Supramolecular complex formation between Rad6 and proteins of the p53 pathway during DNA damage-induced response. *Mol Cell Biol* 2003;23:2463-75.
12. Sanders MA, Brahem G, Nangia-Makker P, Balan V, Morelli M, Kothayer H, et al. Novel inhibitors of Rad6 ubiquitin conjugating enzyme: design, synthesis, identification, and functional characterization. *Mol Cancer Ther* 2013;12:373-83.
13. Eck W, Craig G, Sigdel A, Gerd R, Old LJ, Tang L, et al. PEGylated gold nanoparticles conjugated to monoclonal F19 antibodies as targeted labeling agents for human pancreatic carcinoma tissue. *ACS Nano* 2008; **2**:2263-72.
14. Connor EE, Mwamuka J, Gole A, Murphy CJ, Wyatt MD. Gold nanoparticles are taken up by human cells but do not cause acute cytotoxicity. *Small* 2005; **1**:325-7.
15. Klassen NV, Kedrov VV, Ossipyan YA, Shmurak SZ, Shmyt Ko IM, Krivko OA, et al. Nanoscintillators for microscopic diagnostics of biological and medical objects and medical therapy. *IEEE Trans Nanobioscience* 2009; **8**:20-32.
16. Vigderman L, Zubarev ER. Therapeutic platforms based on gold nanoparticles and their covalent conjugates with drug molecules. *Adv Drug Deliv Res* 2013; **65**:663-76.
17. www.cytimmune.com

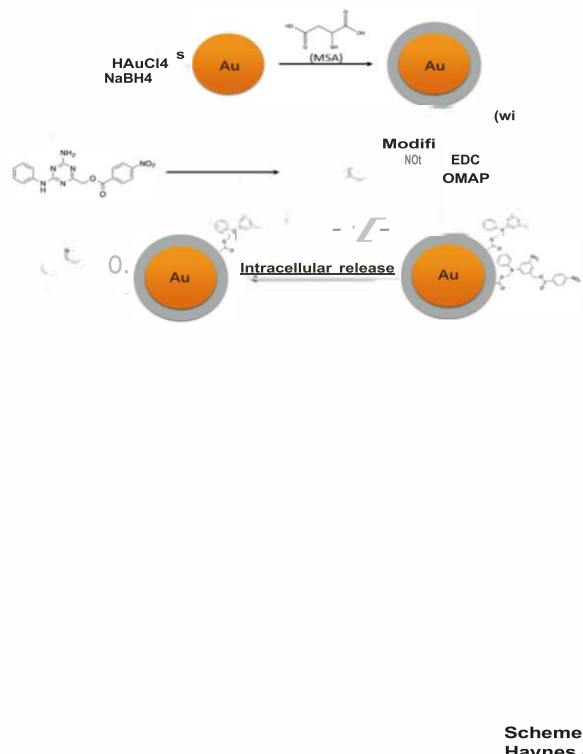
18. Chavez KJ, Garimella SV, Lipkowitz S. Triple Negative Breast Cancer Cell Lines: One Tool in the Search for Better Treatment of Triple Negative Breast Cancer. *Breast Dis* 2010; **32**: 35–48.
19. Turkevich J, Stevenson, PC, Hillier J. A Study of the Nucleation and Growth Processes in the Synthesis of Colloidal Gold. *Discuss Faraday Soc* 1951;55-75.
20. Kimling J, Maier M, Okenve B, Kotaidis V, Ballot H, Plech A. Turkevich method for gold nanoparticle synthesis revisited. *J Phys Chem B* 2006; **110**:15700-7.
21. Frens G. Particle-Size and Sol Stability in Metal Colloids. *Kolloid Z Z Polym* 1972; **250**:736-41.
22. Frens G. Controlled Nucleation for Regulation of Particle-Size in Monodisperse Gold Suspensions. *Nature Phys Sci* 1973; **241**:20-2.
23. Jana NR, Gearheart L, Murphy CJ. Wet chemical synthesis of high aspect ratio cylindrical gold nanorods. *J Phys Chem B* 2001; **105**:4065-7.
24. Sellick CA, Knight D, Croxford AS, Maqsood AR, Stephens GM, Goodacre R, et al. Evaluation of extraction processes for intracellular metabolite profiling of mammalian cells: matching extraction approaches to cell type and metabolite targets. *Metabolomics* 2010; **6**:427-438.
25. Shekhar MP, Tait L, Pauley RJ, Wu GS, Santner SJ, Nangia-Makker P, et al. Comedo-ductal carcinoma in situ: A paradoxical role for programmed cell death. *Cancer Biol Ther* 2008; **7**:1774-82.
26. Khdair A, Gerard B, Handa H, Mao G, Shekhar MP, Panyam J. Surfactant-polymer nanoparticles enhance the effectiveness of anticancer photodynamic therapy. *Mol Pharm* 2008; **5**:795-807.

27. Waheb SIA, Abdul AB, Alzubairi AS, Elhassan MM, Mohan S. In vitro morphological assessment of apoptosis induced by zerumbone on (HeLa). *J Biomed Biotechnol* 2009;2009:769568.
28. Renvoize C, Biola A, Pallardy M, Breard J. Apoptosis: identification of dying cells. *Cell Biol Toxicol* 1998;14:111–20.
29. Cossarizza A, Baccarani-Contri M, Kalashnikova G, Franceschi C. A new method for the cytofluorimetric analysis of mitochondrial membrane potential using the J-aggregate forming lipophilic cation 5,5',6,6'-tetrachloro-1,1',3,3'-tetraethylbenzimidazolcarbocyanine iodide (JC-1). *Biochem Biophys Res Commun* 1993;197:40-5.
30. Dhar S, Lippard SJ. Mitaplatin, a potent fusion of cisplatin and the orphan drug dichloroacetate. *Proc Nat Acad Sci U S A* 2009;106:22199-204.
31. van den Berg A, Dowdy SF. Protein transduction domain delivery of therapeutic macromolecules. *Curr Opin Biotechnol* 2011;22:888–93.
32. Gauthier NC, Monzo P, Kaddai V, Doye A, Ricci V, Boquet P. Helicobacter pylori VacA cytotoxin: a probe for a clathrin-independent and Cdc42-dependent pinocytic pathway routed to late endosomes. *Mol Biol Cell* 2005;16: 4852–66.
33. Gauthier NC, Monzo P, Gonzalez T, Doye A, Oldani A, Gounon P, et al. Early endosomes associated with dynamic F-actin structures are required for late trafficking of *H. pylori* VacA toxin. *J Cell Biol* 2007;177: 343–54.
34. Eto K, Yamashita T, Hirose K, Tsubamoto Y, Ainscow EK, Rutter GA, et al. Glucose metabolism and glutamate analog acutely alkalinize pH of insulin secretory vesicles of pancreatic beta-cells. *Am J Physiol Endocrinol Metab* 2003;285:E262-71.

35. Gulbins E, Teichgräber V, Ulrich M, Endlich N, Riethmüller J, Wilker B, et al. Ceramide accumulation mediates inflammation, cell death and infection susceptibility in cystic fibrosis. *Nat Med* 2008;14:382-91.
36. Mizushima N, Yoshimori T, Levine B. Methods in mammalian autophagy research. *Cell* 2010;140:313-26.
37. Bjorkoy NG, Lamark T, Brech A, Outzen H, Perander M, Overvatn A, et al. P62/SQSTM1 forms protein aggregates degraded by autophagy and has a protective effect on huntingtin-induced cell death. *J Cell Biol* 2005;171:603–14.
38. Pankiv S, Clausen TH, Lamark T, Brech A, Bruun JA, Outzen H, et al. P62/SQSTM1 binds directly to Atg8/LC3 to facilitate degradation of ubiquitinated protein aggregates by autophagy. *J Biol Chem* 2007;282:24131–45.
39. Gao H, Shi W, Freund LB. Mechanics of receptor-mediated endocytosis. *Proc Nat Acad Sci U S A* 2005;102:9469-74.
40. Zhang S, Li J, Lykotrafitis G, Bao G, Suresh S. Size-dependent endocytosis of nanoparticles. *Adv Mater* 2009;21:419-24.
41. Yuan HY, Huang CJ, Zhang SL. Virus-inspired design principles of nanoparticle-based bioagents. *PLoS One* 2010;5:e13495.
42. Yuan HY, Li J, Bao G, Zhang SL. Variable nanoparticle cell adhesion strength regulates cellular uptake. *Phy Rev Lett* 2010;105:1381011-4.
43. Ma X, Wu Y, Jin S, Tian Y, Zhang X, Zhao Y, et al. Gold nanoparticles induce autophagosome accumulation through size-dependent nanoparticle uptake and lysosome impairment. *ACS Nano* 2011;11:8629-39.

44. Shekhar MP, Gerard B, Pauley RJ, Williams BO, Tait L. Rad6B is a positive regulator of beta-catenin stabilization. *Cancer Res* 2008;68:1741-50.
45. Haddad DM, Vilain S, Vos M, Esposito G, Matta S, Kalscheuer VM, et al. Mutations in the intellectual disability gene Ube2a cause neuronal dysfunction and impair parkin-dependent mitophagy. *Mol Cell* 2013;50:831-43.
46. Scovassi IA, Poirier GG. Poly(ADP-ribosylation) and apoptosis. *Mol Cell Biochem* 1999;199:125-37.
47. Chiarugi A. Poly(ADP-ribose) polymerase: killer or conspirator? The 'suicide hypothesis' revisited. *Trends Pharmacol Sci* 2002;23:122-9.
48. Hong SJ, Dawson TM, Dawson VL. PARP and the Release of Apoptosis-Inducing Factor from Mitochondria. Madam Curie Bioscience Database (Internet), Landes Bioscience Austin, TX, 2000-2013.
49. Ha HC, Snyder SH. Poly (ADP-ribose) polymerase is a mediator of necrotic cell death by ATP depletion. *Proc Nat Acad Sci U.S.A.* 1999; 96:13978-13982.
50. Herceg Z, Wang Z-Q. Failure of Poly(ADP-ribose) polymerase cleavage by caspases leads to induction of necrosis and enhanced apoptosis. *Mol Cell Biol* 1999;19:5124-5133.
51. Cipriani G, Rapizzi E, Vannacci A, Rizzuto R, Moroni F, Chiarugi A. Nuclear poly(ADP-ribose) polymerase-1 rapidly triggers mitochondrial function. *J Biol Chem* 2005;280:17227-34.

Figures



Scheme 1,
Haynes et al.

Scheme 1. GNP synthesis, mercaptosuccinic acid (MSA) capping, SMI#9 hydroxymethylation and GNP conjugation.

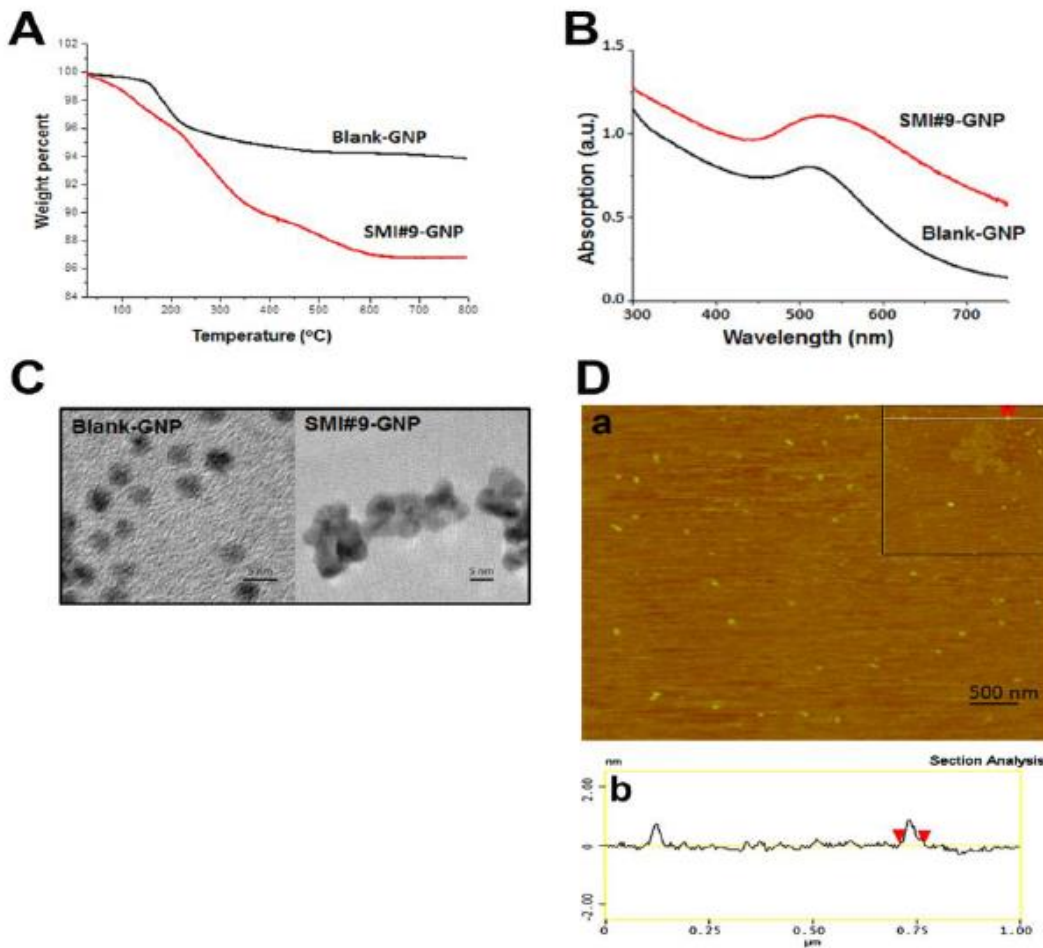


Figure 1
Haynes, et al.

Figure 1. SMI#9-GNP characterization. (A) thermogravimetric analysis; (B) UV-vis spectroscopy; (C) transmission electron microscopy; (D) Atomic force microscopy (AFM). (a), AFM height of SMI#9-GNP, Z-range = 5 nm. Inset in D(a) shows a white line from where the AFM sectional height profile in D(b) was taken, and shows 39 nm particle width (two arrows). (E) FTIR spectra of chloroform/methanol (11:1, v/v) without (green) and with SMI#9 (red). (F) FTIR spectra of SMI#9-GNP treated and control MDA-MB-231 lysates spiked with parent SMI#9. Arrow indicates nitro banding.

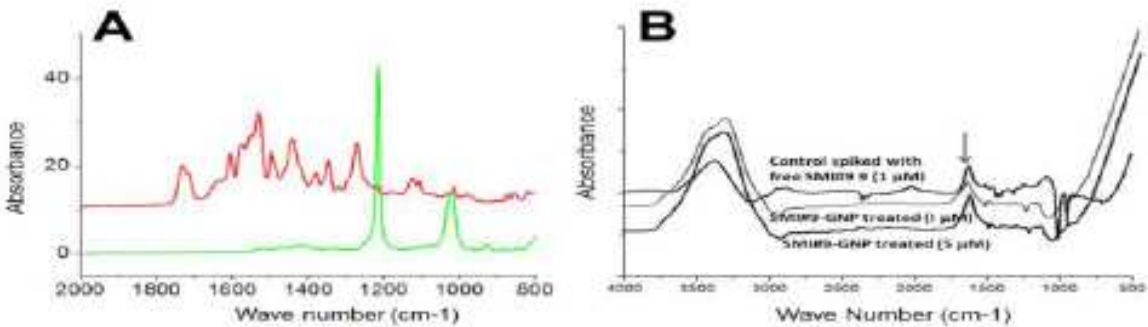


Figure 2.
Haynes et al.

Figure 2. LC-MS/MS analysis of SMI#9 release. A: (a) Chemical structures of parent SMI#9 (MW = 366.1), and GNP-conjugated hydroxymethylated SMI#9 (MW = 396.3). (b) Predicted fragmentation pathway of SMI#9 under the MS condition. (c) Proposed mechanism of SMI#9 release from GNP conjugate. B and C: Chromatograms of SUM1315 extracts prepared at 8 or 24 h from untreated (control), or cells treated with blank-GNP (blank NP), 5 μ M SMI#9 (B), or 5 μ M SMI#9-GNP (C, 9-NP). Samples were monitored at m/Z 366.69 \rightarrow 150.1 for SMI#9 (B) or m/Z 381.3 \rightarrow 150.1 for SMI#9 released from GNP (C).

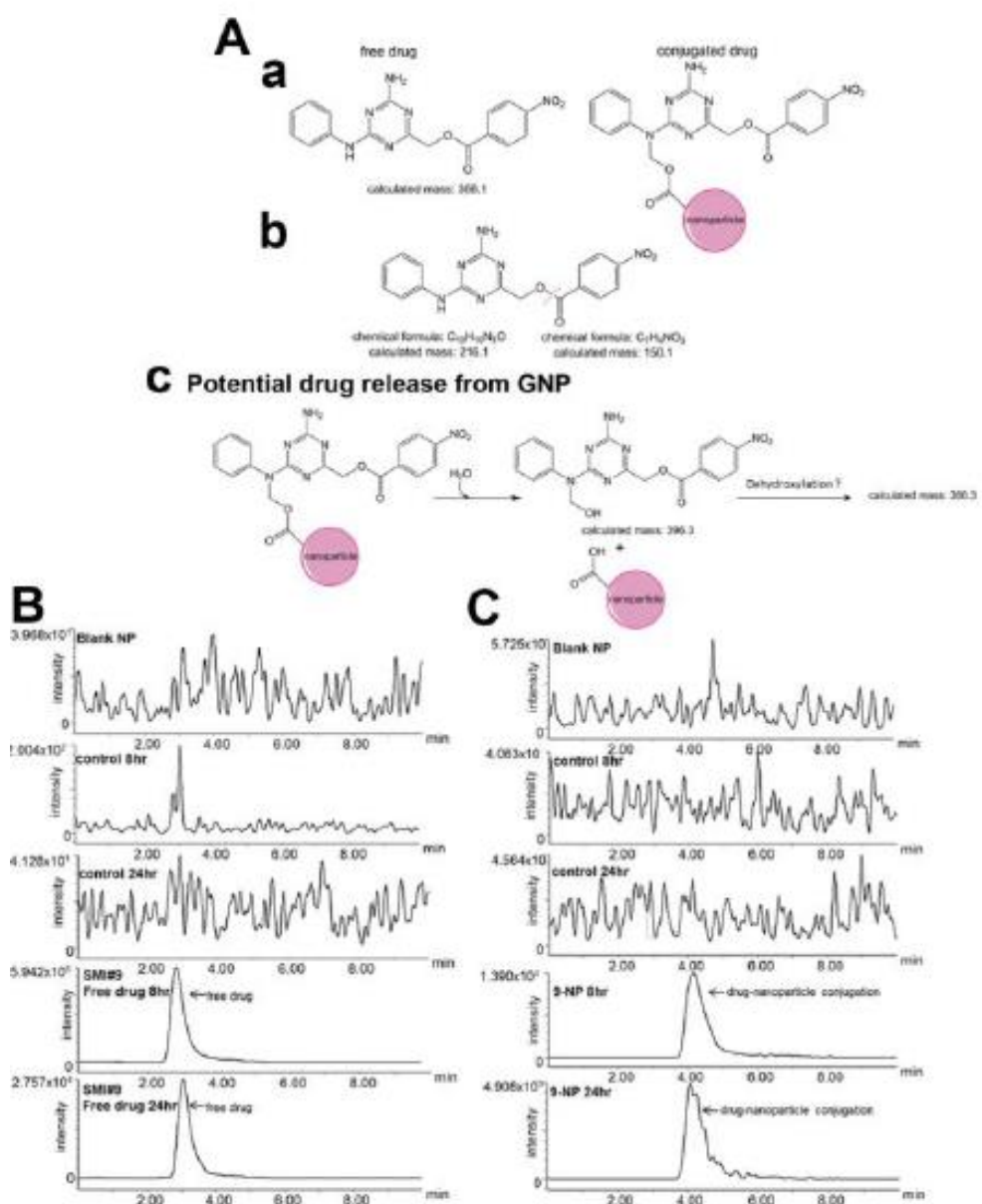


Figure 3
Haynes et al.

Figure 3. SMI#9-GNP sensitivity of TNBC cells. A-D, sensitivities to free or conjugated SMI#9. E, MCF10A cell sensitivity to SMI#9-GNP. Data are mean \pm S.D. F, GI50 values for cisplatin and SMI#9-GNP combination treatments. G, Representative phase contrast micrographs. Note the presence of internalized GNPs in SMI#9-GNP treated SUM1315 cells (inset), and GNP aggregates on HCC1937 cell surface. Original magnification X20.

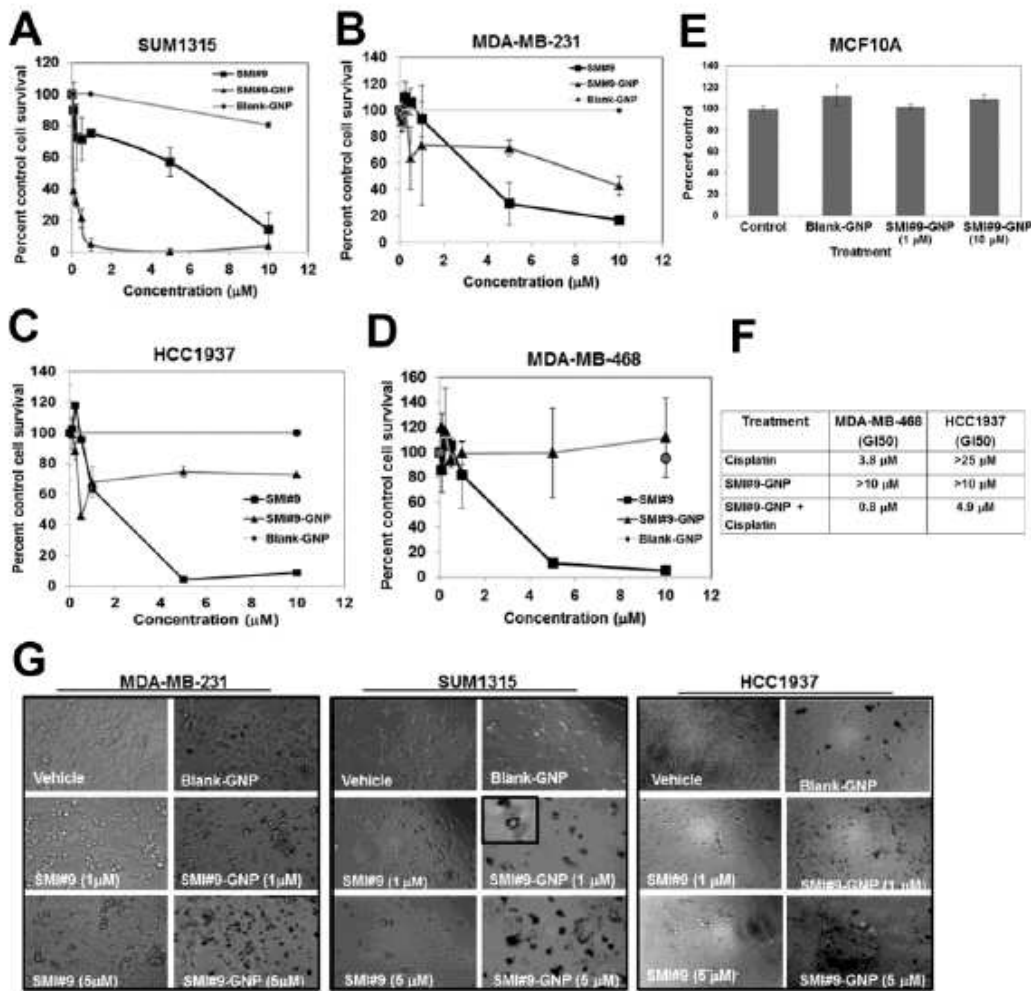


Figure 4
Haynes, et al.

Figure 4. Acridine orange/ethidium bromide staining of SUM1315 (A) and HCC1937 (B) cells, and quantitation of apoptotic/necrotic cells (C, D). JC-1 staining (red, J-aggregates; green, monomers) of SUM1315 cells (E) and HCC1937 (F) cells. Quantitation of mitochondrial potential by manual scoring of SUM1315 (G) or HCC1937 (H) cells containing >5 J-aggregates, and by spectrofluorometry (I). Data are mean \pm S.D. Asterisks, p<0.05. Original magnification, X100.

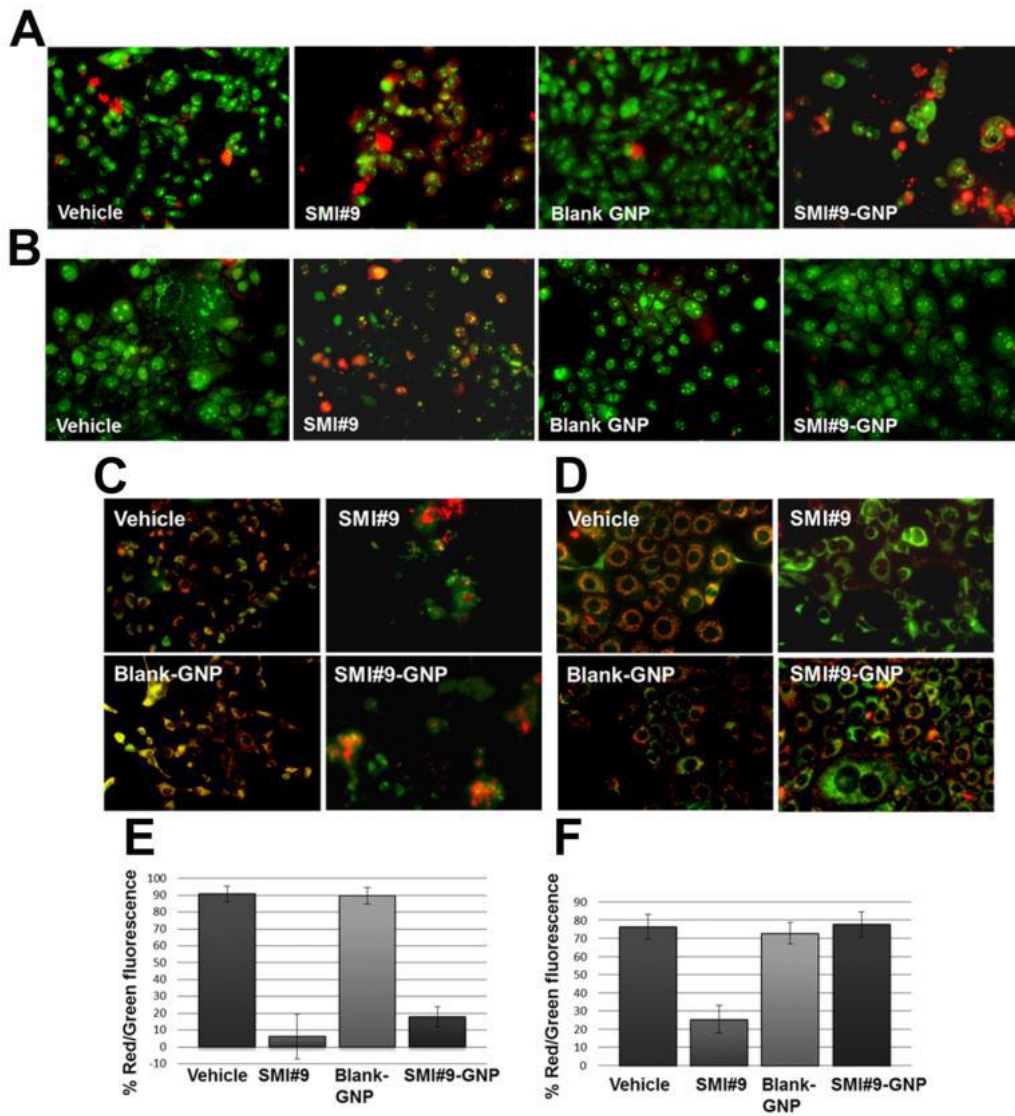


Figure 5,
Haynes et al.

Figure 5. SMI#9-GNP uptake by LysoSensor Green DND-189 staining. Representative images of SUM1315 (A, A', B, B') and HCC1937 (C, D) cells treated with SMI#9-GNP (B, B', D) or untreated (A, A', C). Inset in B, enlarged view of GNP association with lysosomes (arrow). A', B', corresponding phase contrast micrographs of A and B, respectively. Arrow in B' shows acidic vacuoles colocalizing with lysosomes. Scale bar, 5 μ m.

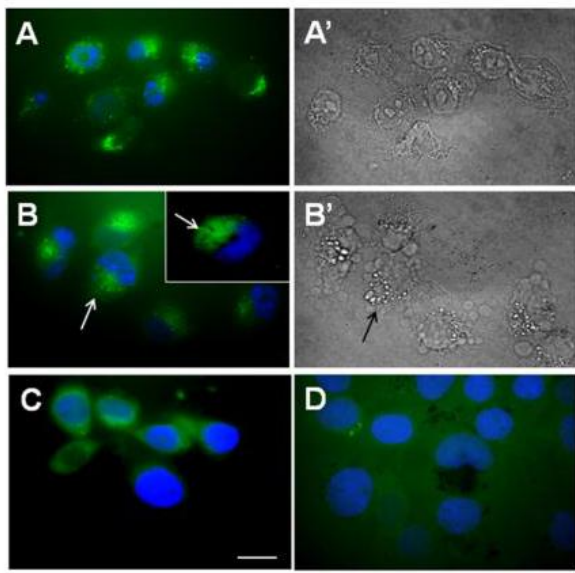


Figure 6
Haynes et al.

Figure 6. SMI#9 and SMI#9-GNP induce PARP-1 stabilization/hyperactivation. A, B, western blot analysis of indicated proteins. Arrows in A and the bracket in B show high molecular weight PARP-1. Blot below B, longer exposure of PARP-1 blot in B. C, phase-contrast micrographs of SUM1315 cells. D, E. LC3 (green) and p62 (red) immunofluorescence staining, respectively, of SUM1315 cells. Cells were stained with DAPI to locate the nucleus. LC-positive dots indicated by arrow. Original magnification X100.

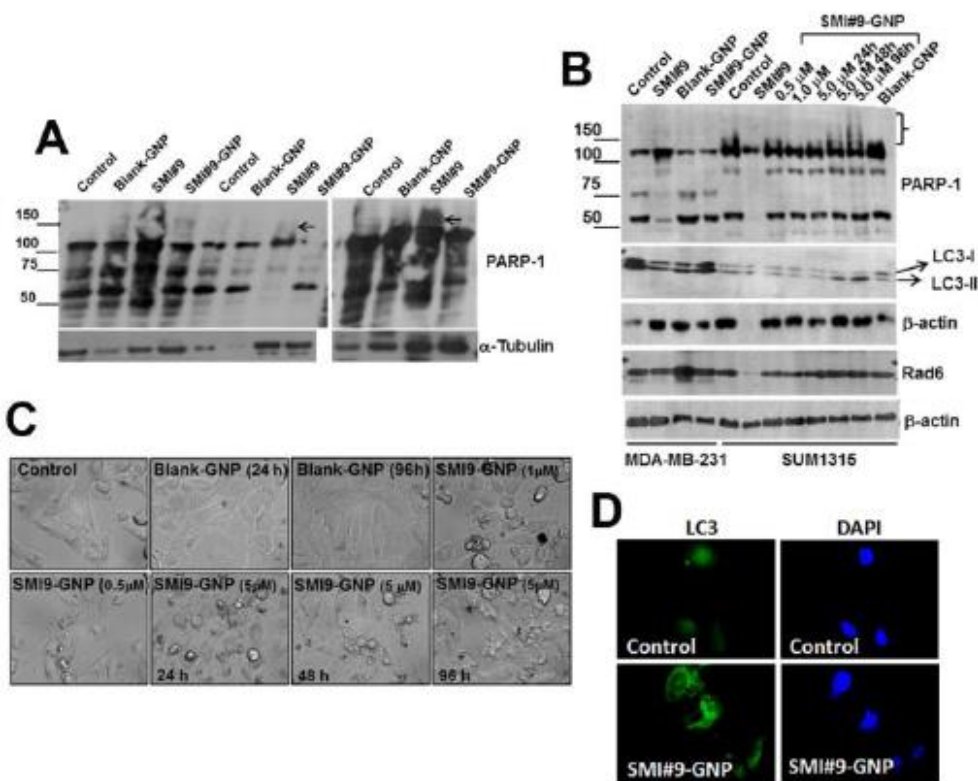


Figure 7
Haynes et al.

Figure 7. Model of SMI#9-induced cell death. Rad6 facilitates autophagic removal of dysfunctional mitochondria. Rad6 inhibition causes accumulation of damaged mitochondria, triggering escalation of autophagy to clear damaged organelles and rescue cell survival. Excessive autophagy combined with mitochondrial permeabilization promotes caspase-dependent or caspase-independent apoptosis. SMI#9 induces PARP-1 stabilization/hyperactivation, which combined with mitochondrial dysfunction contributes to NAD⁺ and ATP depletion and necrosis.